Phonons, magnons, and lattice thermal transport in antiferromagnetic semiconductor MnTe

Sai Mu, Raphael P Hermann, Stéphane Gorsse, Huaizhou Zhao, Michael E. Manley, Randy S. Fishman, Lucas R. Lindsay

Phonons, magnons, and lattice thermal transport in antiferromagnetic semiconductor MnTe

Sai Mu,[1] Raphaël P. Hermann,[1] Stéphane Gorsse,[2,3] Huaizhou Zhao,[4] Michael E. Manley,[1] Randy S. Fishman,[1] and L. Lindsay[1,*]

[1]*Materials Science & Technology Division, Oak Ridge National Laboratory, Oak Ridge, Tennessee 37831, USA*
[2]*CNRS, ICMCB (UMR 5026), Université de Bordeaux, 33600 Pessac, France*
[3]*Bordeaux INP, ENSCBP, 33600 Pessac, France*
[4]*Beijing National Laboratory for Condensed Matter Physics, Institute of Physics, Chinese Academy of Sciences, Beijing 100190, People's Republic of China*

(Received 28 November 2018; published 11 February 2019)

The antiferromagnetic semiconductor MnTe has recently attracted attention for spintronics and high-performance thermoelectric applications. However, little is known about its vibrational and thermal transport properties and how these might relate to the electronic and magnetic structure, particularly as related to 3*d* Mn orbital correlations. Here, we calculate a physically justified Coulomb correlation parameter within the DFT + *U* framework. We couple this framework with the Heisenberg Hamiltonian and first-principles Boltzmann transport to understand the magnetic, vibrational, and phonon thermal transport properties of MnTe. We also perform inelastic neutron and nuclear inelastic x-ray scattering measurements of the total and partial phonon density of states, respectively. Very good agreement is obtained with the measured and calculated phonon density of states, and with available measurements for the band gap, local magnetic moments, Néel temperature, magnon dispersion, thermal conductivity, and phonon dispersion. This study demonstrates that the vibrational and magnetic degrees of freedom are not strongly coupled in MnTe, and provides a more comprehensive picture of this technologically promising material.

DOI: 10.1103/PhysRevMaterials.3.025403

I. INTRODUCTION

Hexagonal MnTe (NiAs type, α phase, hereafter referred to as α-MnTe) is an antiferromagnetic (AFM) transition-metal semiconductor (Néel temperature (T_N) of 307–310 K [1,2]) that has recently attracted attention for its applications in spintronic devices [3,4]. Magnetoresistance measurements have demonstrated that α-MnTe devices possess multiple nonvolatile AFM memory states that are stable even in high magnetic fields [5]. In addition, combining thin-film α-MnTe with a topological insulator has allowed the observation of exchange-biased topological charges arising from coupling with interfacial spins [6]. These antiferromagnetic spintronic systems have unique material behaviors and provide benefits—such as nonvolatility, THz spin dynamics, no fringing stray fields, and stability against magnetic fields—for information technologies (memory logic devices) with the potential to perform beyond Moore's law. However, an accurate theoretical description of the properties of α-MnTe remains a challenge because of the localized and correlated nature of the transition-metal *d* orbitals for which conventional density functional theory (DFT)—either local spin-density approximation (LDA) or the generalized gradient approximation (GGA)—is unable to capture their strong on-site Coulomb repulsion (U).

α-MnTe has also manifested itself as a promising high-performance thermoelectric material, of particular importance for waste heat harvesting and solid-state refrigeration. As the only semiconductor (band gap of 1.27 eV [1,7,8]) in the binary manganese compounds [9], α-MnTe displays an enhanced and practical figure of merit (ZT) via sulfur doping: ZT = 0.65 at 773 K [10]. Moreover, alloying GeTe with MnTe yields an ultralow thermal conductivity (κ) that enhances ZT, attaining a value of 1.61 at 823 K [11]. While the bulk of previous research, particularly theoretical, has focused on the electronic structure [12] and magnetic properties (exchange interactions [13], Néel temperature (T_N) [13], and magnetocrystalline anisotropy [14]), little attention has been paid to lattice dynamical properties and thermal transport. Phonons can play a critical role in determining the functionality and limitations of magnetic semiconductors as they are the primary heat carriers, which is an important factor governing ZT. Phonons can also couple to the electronic and magnetic degrees of freedom. In fact, one mechanism for a thermally driven spin current in the antiferromagnetic insulator Cr_2O_3 is phonon drag via phonon-magnon coupling [15]. Thus, developing a better understanding of phonons and thermal transport derived from accurate and physically meaningful electronic and magnetic structures may provide a means for improving magnetic semiconductor technologies.

In this paper, we systematically examine the electronic, magnetic, vibrational, and thermal transport properties of α-MnTe via a combination of synthesis, inelastic neutron and nuclear inelastic x-ray scattering characterization, and

*Corresponding author: lindsaylr@ornl.gov

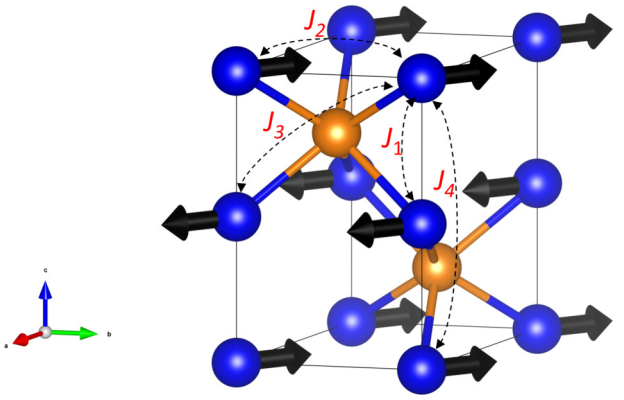

FIG. 1. Crystal structure of hexagonal α-MnTe. Blue spheres are Mn atoms, while orange spheres are Te atoms. Black arrows label the orientations of the Mn local moments (AFM phase here). The exchange parameters (J_n) up to the fourth-nearest-neighbor shell are sketched. Structural illustration is done using VESTA [46].

ab initio electronic structure and lattice dynamical calculations. Computational and experimental details are summarized in Sec. II. Electronic and magnetic properties of α-MnTe are revisited and discussed in Secs. III and IV, respectively. Vibrational properties and thermal transport are discussed and compared with measurements in Sec. V, followed by concluding remarks in Sec. VI.

In particular, this work derives physically justified Coulomb repulsion U, magnetic structure, and exchange parameters from DFT and the quantum spin-5/2 Heisenberg model. This DFT + U method provides reasonable agreement with measurements of phonon and magnon dispersions, the Néel temperature, and thermal conductivity of α-MnTe. Comparison of our measurements and calculations demonstrates that phonons do not strongly couple to the magnetic degrees of freedom of this system. This weak coupling may be beneficial for magnon-based spintronic devices as it prevents phonons from degrading magnon relaxation times and mean free paths. However, having stronger phonon-magnon coupling might improve thermoelectric performance (presumably resulting in shorter phonon and magnon relaxation times, and thus lower thermal conductivity) and improve thermally assisted spin currents via phonon drag, such as in Cr_2O_3 [15].

II. METHODS: THEORY AND EXPERIMENT

Electronic structure. DFT calculations were performed using the projector augmented wave (PAW) method [16] implemented within the Vienna *ab initio* simulation package (VASP) [17,18]. The PAW pseudopotentials correspond to valence electron configurations $3d^6 4s^1$ for Mn and $5s^2 5p^4$ for Te. We used the primitive cell shown in Fig. 1 for all calculations except for those involving complicated magnetic configurations, where a $2 \times 2 \times 2$ supercell built from the four-atom hexagonal unit cell was employed. For all calculations, measured room temperature lattice parameters were used: $a = 4.15$ Å and $c = 6.71$ Å [19,20]. The exchange-correlation functional was treated within the GGA [21] with energy cutoff for the plane-wave expansion set to 520 eV. Γ-centered Monkhorst-Pack k-point grids [22] were used for the Brillouin zone integrations. The electronic structure of the primitive cell was calculated using a tetrahedral method on a $6 \times 6 \times 4$ k-point mesh. The AFM ground state (spins parallel in-plane, but antiparallel between adjacent planes (see Fig. 1) was employed for most calculations.

TABLE I. Exchange parameters (J_n meV, where n denotes the nth-neighbor shell of an Mn atom) fitted using the total energies of 28 different magnetic configurations at $U_{eff} = 4.8$ eV. As defined, negative J_n indicates the antiferromagnetic coupling. z_n is the corresponding coordination and r_n denotes the bond length (Å). The last two columns give the Néel temperature (T_N K) of AFM α-MnTe from the exchange parameters using the quantum pair-cluster (PC) approximation and the quantum mean-field (MF) approximation. The measured T_N is 307–310 K [1,2].

	J_1	J_2	J_3	J_4	T_N (PC)	T_N (MF)
$U = 4.8$ eV	–19.2	–0.17	–2.5	–1.0	306	354
Expt. [9]	–23.1	0.72	–3.1	N/A	396	475
z_n	2	6	12	2	N/A	N/A
r_n	3.36	4.15	5.34	6.72	N/A	N/A

The Coulomb correlations within the $3d$ shells of the transition-metal Mn ions were described using the spherically averaged GGA + U method [23]. This requires a single adjustable effective Coulomb correlation parameter: $U_{eff} = U - J$, where J is the on-site exchange parameter (typically $\sim$1 eV) as input to the Hamiltonian. To give U_{eff} a physical basis, we employed a linear response method [24] for which a small perturbation of the potential (δV) on a single Mn site within the primitive cell is applied, and the resulting bare charge response (δn_0, without optimizing the charge density) and screened response (δn, with the charge density fully relaxed) are calculated. The effective Coulomb correlation is obtained from $U_{eff} = \delta V/\delta n_0 - \delta V/\delta n$ and is found to be 4.8 eV for the $3d$ orbitals of α-MnTe.

Magnon spectra. Eigenvalues of the spin-wave excitations based on the Heisenberg Hamiltonian ($S = 5/2$) were obtained from the diagonalization of the following (non-Hermitian) 4×4 $\mathcal{L}(\boldsymbol{q})$ matrix in the basis of creation and annihilation operators on two Mn sublattices ($a^1_{\boldsymbol{q}}, a^2_{\boldsymbol{q}}, a^{1\dagger}_{-\boldsymbol{q}}, a^{2\dagger}_{-\boldsymbol{q}}$) [25,26]:

$$\mathcal{L}(\boldsymbol{q}) = \begin{pmatrix} A_{\boldsymbol{q}} & 0 & 0 & -B_{\boldsymbol{q}} \\ 0 & A_{\boldsymbol{q}} & -B_{\boldsymbol{q}} & 0 \\ 0 & B_{\boldsymbol{q}} & -A_{\boldsymbol{q}} & 0 \\ B_{\boldsymbol{q}} & 0 & 0 & -A_{\boldsymbol{q}} \end{pmatrix}, \quad (1)$$

with $A_{\boldsymbol{q}} = (S/2)(\sum_{n\in\mathrm{FM}} z_n J_n[1 - \Gamma_n(\boldsymbol{q})] - \sum_{n\in\mathrm{AFM}} z_n J_n)$ and $B_{\boldsymbol{q}} = -(S/2)(\sum_{n\in\mathrm{AFM}} z_n J_n \Gamma_n(\boldsymbol{q}))$, where z_n is the coordination number of the nth-nearest-neighbor shell (see Table I) and $\Gamma_n(\boldsymbol{q}) = (1/z_n)\sum_{\boldsymbol{d}_{nj}} e^{i\boldsymbol{q}\boldsymbol{d}_{nj}}$ is the magnetic form factor, with $\boldsymbol{d}_{nj}$ the vector between the interacting atoms—central atom and the jth atom within the nth-neighboring shell. As illustrated in Fig. 1, the sum over couplings between ferromagnetic (FM) aligned spins includes J_2 and J_4, while the sum over couplings between AFM aligned spins includes J_1 and J_3.

Phonons and lattice thermal conductivity (κ). Harmonic (phonons) and third-order anharmonic (three-phonon interactions) [27,28] interatomic force constants (IFCs) were

calculated using the conventional supercell method based on a 4 × 4 × 3 supercell of α-MnTe in both AFM and ferromagnetic (FM) collinear states. An interaction cutoff radius for the anharmonic IFCs of 5.5 Å was employed, while harmonic IFCs were determined for all interactions within the supercell. This cutoff radius is typical compared to previous calculations of converged thermal conductivity values for bulk semiconductors [29,30]. Translational invariance was enforced for both harmonic and anharmonic IFCs [29]. The lattice thermal conductivity is given by [27,28]

$$\kappa_\alpha = \sum_{\boldsymbol{q}j} C_{\boldsymbol{q}j} v^2_{\boldsymbol{q}j\alpha} \tau_{\boldsymbol{q}j\alpha}, \tag{2}$$

where $C_{\boldsymbol{q}j}$ is the volumetric mode specific heat for a phonon with wave vector $\boldsymbol{q}$ and branch index j, $v_{\boldsymbol{q}j\alpha}$ is the phonon speed in Cartesian direction α, and $\tau_{\boldsymbol{q}j\alpha}$ is the phonon transport lifetime when a temperature gradient is applied in the αth direction. $\tau_{\boldsymbol{q}j\alpha}$ is determined by full solution of the Peierls-Boltzmann transport equation [27,28,31–33] with scattering probabilities for three-phonon [27,28,31–33] and phonon-isotope [34] (mass variations due to natural isotope abundances) interactions determined from quantum perturbation theory, with no adjustable empirical parameters. Due to the hexagonal structure, the thermal conductivity of α-MnTe has two nontrivial components: along the hexagonal planes, κ_{in}, and perpendicular to the planes along the c axis, κ_{out}.

MnTe synthesis. A sample with the nominal compositions of $Mn_{0.97}Li_{0.03}Te$ was synthesized for neutron scattering by ball milling the raw elements (Mn powder 99.99%, Li chunks 99.9%, Te chunks 99.999%) within an argon-filled stainless-steel jar using a high-energy ball milling machine (SPEX 8000D). The materials were milled for 8 h and then hot pressed at 1173 K for 20 min by spark plasma sintering (SPS) under an axial pressure of 40 MPa with a heating rate of 50 K/min. The sample is disk shaped, 12.7 mm in diameter, ∼25.4 mm in thickness, and with a density not less than 97% of the theoretical value. The Li dopants were added to stabilize the phase against decomposition. Separately for the Te-125 nuclear inelastic scattering, ∼100 mg of a polycrystalline MnTe ingot was synthesized by induction melting a mixture of high-purity elements Mn (99.9%), with a small Mn excess to prevent the formation of Te bearing impurities, and 95% isotopically enriched Te-125 in a glassy carbon crucible enclosed in an evacuated quartz tube. The addition of lithium is not practical for this small-scale synthesis. Melting was performed several times to ensure good homogeneity. The sample was sent to the synchrotron radiation facility in a sealed ampoule and measured within two days of synthesis in order to avoid possible decomposition. Neutron and x-ray diffraction are shown in the Supplemental Material [35] for the $Mn_{0.97}Li_{0.03}Te$ and $Mn^{125}Te$ samples, respectively.

Inelastic scattering. Inelastic neutron scattering data were recorded at the ARCS spectrometer of the Spallation Neutron Source with incident neutron energies of 60 meV at a temperature of 250 K, below the magnetic transition, on a pressed polycrystalline sample of 25 g of $Li_{0.03}MnTe$. The Li contribution to the generalized phonon density of states (GDOS) was neglected as it is expected to contribute only about 5% to the vibrational states, and mostly as impurity modes at energies above the phonon cutoff due to the light Li mass. The data were analyzed in the incoherent scattering approximation by summing up data collected between 6 and 8.5 $Å^{-1}$. The lower scattering vector range, between 2.5 and 3 $Å^{-1}$, was used to remove any residual magnon contribution. The obtained inelastic scattering function $S(E)$ (see Supplemental Material [35]) was then further reduced to a GDOS by subtracting the multiphonon contribution. This was carried out with a modified version of the DOS software [36] by utilizing an average recoil energy of 1.8 meV which provided the best self-consistent GDOS.

The partial Te-specific DOS was obtained by recording the Te-125 nuclear inelastic scattering signal on the $Mn^{125}Te$ sample with 95% isotopic Te enrichment. Note that this method is sensitive only to Te vibrations and is insensitive to non-Te-based impurities. The data were recorded at 25 K utilizing the backscattering monochromator of the beam line ID22N, ESRF [37]. Multiphonon correction and DOS extraction from the scattering function $S(E)$ (see Supplemental Material [35]) were also carried out by the DOS software [36]. In order to estimate the Mn-element-specific DOS, the Te-element-specific DOS was subtracted from the GDOS obtained by inelastic neutron scattering using the weighted cross sections of 48% for the Te scattering and 52% for the Mn scattering. A norm-conserving scaling of 3% hardening was applied to the GDOS before subtraction in order to account for small softening occurring between 25 and 250 K. Note that the x-ray diffraction data (see Supplemental Material [35]) indicates that the MnTe powder exhibits a mild platelet habit with about 10% excess preferential orientation of the powder in the c axis. As a consequence, the obtained Te partial DOS is likely deviated somewhat from a perfect powder average. The calculated MnTe DOS (partial and total) projected along different directions are given in the Supplemental Material [35].

III. ELECTRONIC STRUCTURE

To reasonably describe the vibrational and magnetic properties of α-MnTe, an accurate description of the electronic structure is necessary. Conventional DFT predicts α-MnTe is a metal rather than a semiconductor [12]. To account for this in previous work, GGA + U has been employed to include Coulomb repulsion [13,14], but with U as a semiempirical parameter. Given that many material properties (e.g., band gap, local moments, exchange interactions, phonon frequencies) are sensitive to U [13], it is desirable to establish a reliable and physically meaningful Coulomb correlation. Thus, we employed a linear response method—difference of the bare charge and screened charge responses as a function of the on-site potential shift as described above—to compute the Coulomb correlation U_{eff}. The bare response contributes 8 eV to U_{eff}, while electronic relaxation gives a competing contribution of −3.2 eV, giving $U_{\text{eff}} = 4.8$ eV (see Supplemental Material [35]). This calculated value is greater than those employed in Refs. [13] and [14] (4 and 3.1 eV, respectively) used to reproduce the measured T_N of α-MnTe based on quantum mean-field (MF) theory. Our calculated value is closer to that given in Ref. [38], $U_{\text{eff}} = U - J = 5.3$ eV, for which U_{eff} was evaluated using the Slater's transition-state

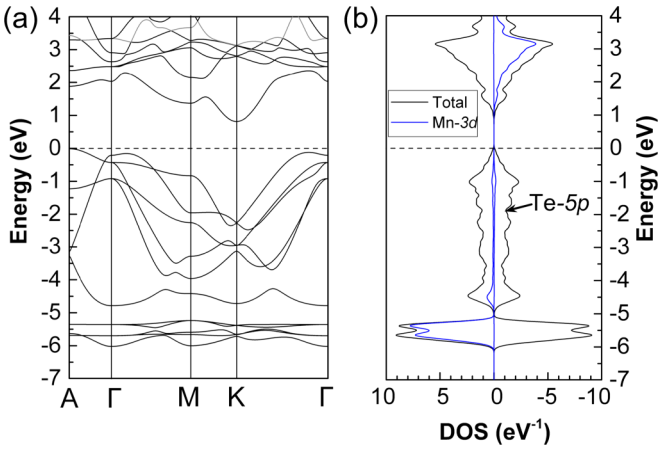

FIG. 2. (a) Calculated band structure in high-symmetry directions of AFM α-MnTe. Each band is doubly degenerate. (b) Spin-resolved total (black curves) and partial (Mn-3d, blue curves) density of states. The electronic structures are calculated within GGA + U using $U_{eff} = 4.8$ eV.

method. The large U_{eff} calculated here is reasonable given that there are five 3d electrons (half filled) on one Mn^{2+} cation. We note that the LDA gives a similar value: $U_{eff} = 4.9$ eV.

The calculated electronic band structure and density of states (DOS) are shown in Fig. 2. First, an indirect band gap—0.8 eV from A to K points—is observed, which is smaller than that obtained from measurements (∼1.3 eV) [1,7,8] and similar to a previous theoretical result (∼0.8 eV) [39]. Our LDA calculations give similar band structure features, though a reduced band gap (0.6 eV) compared with GGA. Both the valence-band maximum—A point—and the conduction-band minimum—K point—are Te 5p states. The underestimated gap is likely caused by underestimation of the binding energies of the p orbitals, a well-known DFT deficiency when describing insulators and semiconductors [40].

IV. MAGNETIC PROPERTIES

The Mn 3d shell is half filled with a relatively large exchange splitting (7 eV). As seen in Fig. 2(b), the on-site exchange between the filled and unfilled 3d orbitals is mediated by Te 5p states (lying between), epitomizing the superexchange mechanism. Employing $U_{eff} = 4.8$ eV, the calculated local moment on Mn sites in the ground state is about 4.55 μ_B, consistent with previous work: 4.76 μ_B [22], 4.66 μ_B [21], 4.27 μ_B [14], 4.52 μ_B [11]. The total energies of 28 different spin configurations including the long-range FM state, different types of AFM states, and other random collinear spin arrangements were calculated from DFT and were fitted to the conventional Heisenberg Hamiltonian,

$$H = -\frac{1}{2}\sum_{i,j\in n\text{th shell}} J_n \boldsymbol{e}_i \cdot \boldsymbol{e}_j, \tag{3}$$

with exchange parameters (J_n) included up to fourth-nearest neighbors ($n = 4$). Consistent with experiments and previous theoretical work [13], the AFM state illustrated in Fig. 1 is the most energetically favorable. Figure 1 depicts the exchange paths J_1 to J_4: J_1 is the nearest exchange coupling between intersublattices in different planes, while J_2 is the second-nearest coupling between intrasublattices in the same plane. The fitted exchange parameters are listed in Table I. All the exchange parameters are antiferromagnetic. The J_1 and J_3 intersublattice exchanges are dominant and thus determine the AFM ground state, while J_2 (surprisingly weak) and J_4 represent frustrated exchange interactions. The dominant J_1 and J_3 terms ensure AFM coupling between Mn pairs on adjacent planes. This then enforces ferromagnetic coupling between second-nearest Mn neighbors on the same plane. The fidelity of the fitting is verified by the "take-one-out" cross-validation score (CV, meV). The CV score of ∼8.6 meV/cell is small compared with the range of magnetic energies ($\Delta E \sim$ 1090 meV/cell) of the 28 spin configurations sampled, indicating a reliable fitting quality and a well-represented Heisenberg model to fourth-nearest exchange interaction. If J_4 is not included in the fitting, a larger CV (13.6 meV/cell) is obtained and J_2 is slightly enhanced, while J_1 and J_3 are relatively unchanged. As demonstrated in Table I, our fitted exchange parameters are in generally good agreement with measurements [9]. Theory slightly underestimates J_1 and J_3, and experiment gives a stronger, ferromagnetic J_2, albeit smaller than the other exchange parameters.

Previously, magnetism in α-MnTe was understood as the exchange of Mn 3d orbitals mediated by filled Te 5p bands: superexchange mechanism [9]. However, here we find the direct hopping of 3d electrons (direct-exchange mechanism) also contributes to the total AFM exchange, particularly for the nearest coupling J_1. For a half-filled d shell, the direct exchange also favors AFM spin alignment that gives an energy gain ($\sim -t^2/U$ where t is the hopping integral) from the hopping of the d orbitals. The nearest Mn-Mn bond length is only 3.56 Å, and thus direct electron hopping (orbital hybridization) is likely. This is supported by calculations of the charge density of the t_{2g} orbitals, showing orbital overlap between nearest Mn pairs [13]. In addition, the demonstrated sensitivity of J_1 to U accompanied by reduced orbital overlapping [13] indicates an appreciable contribution from direct exchange. This also suggests that a tensile epitaxial strain on MnTe thin film, accompanied by reducing the nearest Mn-Mn bond length after relaxation, will give stronger antiferromagnetic J_1 and thus a higher Néel temperature, which is good for its practical applications. We also verified the J_1 sensitivity: reducing U_{eff} by 1 eV increases the magnitude of J_1 by 24%. Furthermore, Mn-Te-Mn bond angles for the nearest Mn pairs are only 71° (relatively close to 90°) and, according to the Goodenough-Kanamori-Anderson (GKA) rule [41,42], the antiferromagnetic superexchange is expected to be weak due to small orbital overlap. Moreover, the extremely weak $J_2(J_2/J_1 = 0.8\%)$ is understood by the fact that the corresponding Mn-Te-Mn bond angle is about 90.4°, greatly suppressing the antiferromagnetic superexchange. The pronounced J_3 can be understood based on the Mn-Te-Mn angle and GKA.

Based on the calculated exchange parameters listed in Table I, the Néel temperature is evaluated using the quantum $S = 5/2$ pair-cluster (PC) approximation [43]. Our calculated $T_N^{PC} = 306$ K is in excellent agreement with the measured $T_N^{expt} = 307 - 310$ K [1,2], indicating that the essential details of the electronic and magnetic structure of α-MnTe are well

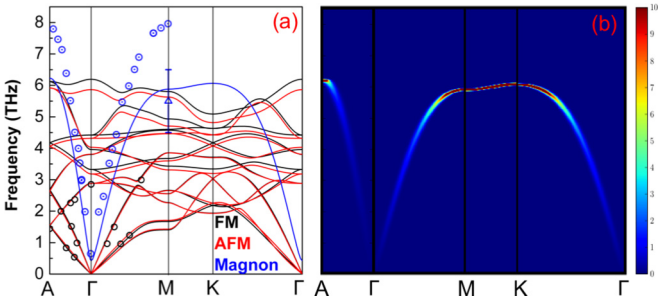

FIG. 3. (a) Calculated magnon (blue curves) and phonon (red curves) dispersions of α-MnTe in the AFM state using $T = 300$ K measured lattice parameters. Measured data are also shown for magnons at $T = 11$ K (blue circles) [32], an M-point magnon at $T = 300$ K (blue triangle), and phonons at $T = 300$ K (black circles) [43]. Phonon dispersion for the FM state is given by black curves. (b) Calculated inelastic spectra [$S(\boldsymbol{q}, \omega)$, arbitrary units] of AFM α-MnTe in zero magnetic field with $S = 5/2$ and J_0 to J_4 from Table I.

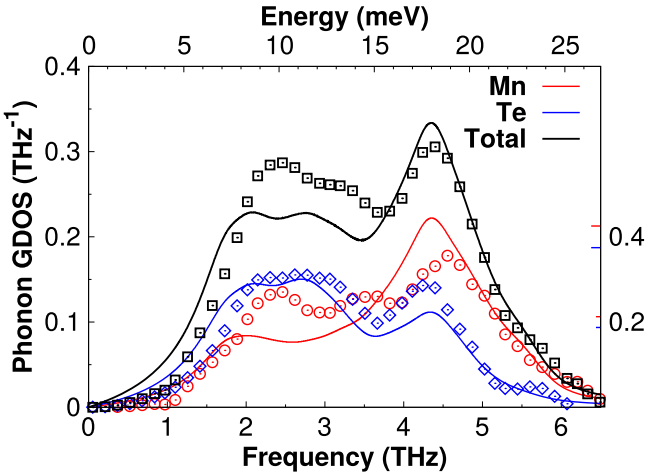

FIG. 4. Measured (symbols) and calculated (curves) total (black) and partial phonon density of states (DOS) of α-MnTe in the AFM state for Mn vibrations (red) and Te vibrations (blue). The total GDOS is neutron weighted and normalized to unity; red and blue tics on the right axis indicate scaling for the normalized-to-unity partial DOS for Mn and Te, respectively. A 3% scaling (see text) was applied to the total GDOS data.

captured by the $GGA + U$ approximation. We note that a previous quantum $S = 5/2$ mean-field approximation [43] gave an overestimated $T_N^{MF} = 354$ K due to the neglect of pairwise correlations.

Magnetic susceptibility measurements [37] of α-MnTe give a Curie-Weiss temperature $\Theta_{CW} = 583$ K, compared with $T_N^{MF} = 354$ K. We can write $T_N^{MF} \sim aJ_s$ and $\Theta_{CW} \sim aJ_0$, where $J_s = \sum_{j \in n\text{th shell}} \boldsymbol{e}_i \cdot \boldsymbol{e}_j J_n$ is the stagger sum of the exchange parameters, $J_0 = \sum_n J_n$ is the plain sum, and a is a common factor. Deviation of T_N^{MF}/Θ_{CW} (and thereby $J_s/|J_0|$) from 1 indicates the importance of intrasublattice exchange coupling (J_2 and J_4). A relatively small T_N^{MF}/Θ_{CW} value of 0.61 for α-MnTe suggests a notable contribution from the intrasublattice exchange, where the ratio of the total intersublattice and the total intrasublattice exchange is 4, while the same ratio from DFT-fitted J_n is 22. This suggests that the DFT calculations underestimate the intrasublattice exchange.

Figure 3(a) gives the calculated spin-wave (magnon) dispersion for the AFM state of α-MnTe compared with measured dispersion data at $T = 11$ K [32] and a single data point at $T = 300$ K [43]. Also given are the calculated and measured [43] phonon dispersions. All calculated values are derived from the measured lattice parameters of α-MnTe at $T = 300$ K using $U_{eff} = 4.8$ eV. The sensitivity of the spin-wave dispersion to the lattice parameters and varying U_{eff} are shown in the Supplemental Material [35]. Figure 3(b) gives the simulated inelastic spectra [$S(\boldsymbol{q}, \omega)$] of AFM α-MnTe in zero magnetic field. An analytical expression of the spin-wave dispersion from the Heisenberg Hamiltonian described above ($\omega_q^2 = A_q^2 - B_q^2$) gives doubly degenerate magnon branches in the absence of magnetic anisotropy. If the easy-plane anisotropy, $\sum_i K(\boldsymbol{e}_i^z)^2$, is introduced to Eq. (3), the expression for the spin-wave dispersion is modified by replacing B_q with $B_q \pm K/S^2$, where K represents the easy-plane anisotropy which is taken from experiment [9]. Kinks and anomalies associated with strong coupling of phonons and magnons, particularly where their energy scales coincide, are not observed in the measured or in the calculated dispersions. The absence of such behavior suggests that the vibrational and magnetic degrees of freedom are not strongly coupled. Furthermore, the calculated vibrational properties (phonon dispersion and conductivity) for MnTe derived separately for AFM and FM magnetic states are nearly identical (see Sec. V), also suggesting weak coupling.

V. PHONON PROPERTIES

Phonon dispersion and DOS. The calculated and measured phonon dispersions in Fig. 3(a) are in good agreement for AFM α-MnTe. We note that the calculated dispersions (phonon and magnon) are not temperature dependent, but are calculated using the experimental $T = 300$ K lattice structure, while the measured phonon dispersion was performed at $T = 300$ K. α-MnTe has a second-order magnetic phase transition from the AFM state ($T_N^{expt} \sim 307-310$ K [1,2] measured; $T_N^{PC} = 306$ K calculated here), above which it is in a paramagnetic state. The lattice dynamical and phonon transport properties of this paramagnetic state are expected to be bounded by those in the AFM and FM states since the renormalized IFCs are bounded by these [44]. Thus, we also calculated the phonon dispersion of α-MnTe in the FM state for comparison. The acoustic modes for the AFM and FM states are nearly indistinguishable, while the optic modes are generally shifted to higher frequencies by a couple of percent. The calculated and measured phonon DOS for AFM α-MnTe from this work are shown in Fig. 4, with total and Mn- and Te-projected vibrations shown separately. Calculated DOS data are determined by Brillouin zone integration with a dense mesh of k points and Lorentzian smearing with 1 meV width. The total GDOS is normalized to give a neutron weighted area of unity under the curve. General features and magnitudes of the calculated and measured DOS are in very good agreement, particularly for the Te-projected DOS. Some calculated spectral weight is missing at midfrequency for the Mn vibrations. This discrepancy may be attributed to a combination of not explicitly considering thermally

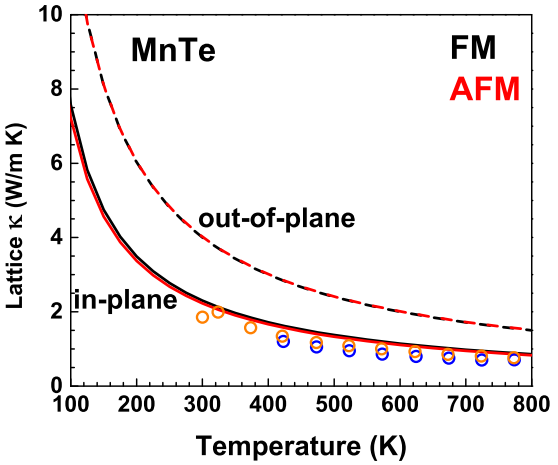

FIG. 5. Calculated lattice thermal conductivity (curves) of α-MnTe compared with measured data (orange circles [47] and blue circles [10]) in the paramagnetic state. Black curves correspond to α-MnTe in the AFM state, while red curves correspond to the FM state. Solid curves give the in-plane conductivity (κ_{in}), while dashed curves give the cross-plane conductivity (κ_{out}).

dependent vibrational properties in the calculations (e.g., lattice expansion, anharmonic phonon renormalization) and of the small preferential orientation in the measured Te partial DOS discussed above. We note that the Mn partial DOS is inferred from direct measurements of the GDOS and partial Te DOS on two different samples at different temperatures.

Phonon thermal conductivity. Figure 5 gives the calculated phonon thermal conductivity (κ_{in} and κ_{out}) for α-MnTe as a function of temperature. Again, above $T_{\text{N}}^{\text{expt}} = 307$–$310$ K, α-MnTe is in a paramagnetic state. Thus, below T_N, the calculated AFM κ curve (black) gives the more accurate representation of κ of α-MnTe. We also present κ with harmonic and anharmoinc IFCs calculated in the FM configuration (red); however, very little difference is observed in κ_{in} and κ_{out} over the temperature range considered. Again, calculated κ values of the paramagnetic state above room temperature are expected to be bounded by the FM and AFM curves. Thermal transport in α-MnTe is significantly anisotropic with $\kappa_{\text{out}}/\kappa_{\text{in}} = 1.8$ at room temperature, partly due to the larger sound speed in the cross-plane direction 1530 m/s over that in the plane 1290 m/s, partly due to larger optic mode contributions to κ in the cross-plane direction. The calculations for the in-plane κ are just above the available measured data. Considering the relatively simple structure of α-MnTe, the room temperature $\kappa_{\text{in}} = 2.23$ W/m K is quite low, comparable to the prominent thermoelectric material PbTe, 2.37 W/m K [45].

Given the reasonable agreement with this measured κ data, we draw two conclusions: (1) The spin disorder induced by thermal spin fluctuations in the paramagnetic state does not provide significant scattering resistance to the phonons. This is consistent with the lattice vibrations not interacting strongly with the magnetic structure. (2) Magnon thermal transport is not relevant in this temperature range since the collective (long-range) spin exciations are only valid below a temperature $\sim$0.1–0.2 T_{N}. Above T_N, long-range spin correlations do not exist and thermal spin fluctuations are not anticipated to significantly mediate heat transport. In contrast, the (diffusive) paramagnon-assisted thermal transport, in the presence of magnetic short-range order, may be nontrivial above T_N and therefore worthy of investigation. However, this is beyond the scope of the current study.

VI. SUMMARY AND CONCLUSIONS

In summary, we have critically examined the electronic, magnetic, vibrational, and thermal transport properties of the antiferromagnetic semiconductor α-MnTe via joint computational and experimental efforts. In particular, we employed GGA + U density functional theory (DFT) calculations for electronic structure, a spin-5/2 Heisenberg Hamiltonian, and various magnetic configurations to describe magnetic properties, and a Boltzmann transport equation methodology to describe phonon transport. Furthermore, we synthesized α-MnTe and employed inelastic neutron scattering to determine the phonon density of states (DOS) for comparison with DFT calculations. A physically meaningful Coulomb correlation parameter was determined from linear response, and subsequent DFT calculations with different magnetic configurations were employed to determine magnetic exchange parameters, the Néel temperature, magnon and phonon dispersions, vibrational DOS, and lattice thermal conductivity. Overall, reasonable agreement of these with measured values is attained and a more comprehensive physical picture of the combined properties of α-MnTe is developed. The results presented here suggest that direct coupling of vibrational and magnetic degrees of freedom in this material is weak.

ACKNOWLEDGMENTS

This work was supported by the U.S. Department of Energy (DOE), Office of Science, Basic Energy Sciences, Materials Sciences and Engineering Division. Portions of this research used resources at the Spallation Neutron Source, a U.S. DOE Office of Science User Facility operated by the Oak Ridge National Laboratory and beam line ID22N at the European Synchrotron Radiation Facility (ESRF), Grenoble, France. Dr. Ilya Sergueev and Dr. Paula Fichtl are acknowledged for support during data acquisition at ID22N, SNS. Dr. Douglas Abernathy is acknowledged for support during data acquisition at ARCS, SNS. H.Z. acknowledges the funding support from the National Natural Science Foundation of China (NSFC) under Grants No. 51572287 and No. U1601213.

[1] C. Ferrer-Roca, A. Segura, C. Reig, and V. Munoz, Phys. Rev. B **61**, 13679 (2000).
[2] K. Walther, Solid State Commun. **5**, 399 (1967).
[3] T. Jungwirth, X. Marti, P. Wadley, and J. Wunderlich, Nat. Nanotechnol. **11**, 231 (2016).
[4] V. Baltz, A. Manchon, M. Tsoi, T. Moriyama, T. Ono, and Y. Tserkovnyak, Rev. Mod. Phys. **90**, 015005 (2018).
[5] D. Kriegner, K. Výborný, K. Olejník, H. Reichlová, V. Novák, X. Marti, J. Gazquez, V. Saidl, P. Němec, V. V Volobuev *et al.*, Nat. Commun. **7**, 11623 (2016).

[6] Q. L. He, G. Yin, A. J. Grutter, L. Pan, X. Che, G. Yu, D. A. Gilbert, S. M. Disseler, Y. Liu, P. Shafer, B. Zhang, Y. Wu, B. J. Kirby, E. Arenholz, R. K. Lake, X. Han, and K. L. Wang, Nat. Commun. **9**, 2767 (2018).

[7] G. Zanmarchi and C. Haas, Philips Res. Rep. **23**, 389 (1968).

[8] J. D. Wasscher, Philips Res. Rep., Suppl. (1969).

[9] W. Szuszkiewicz, E. Dynowska, B. Witkowska, and B. Hennion, Phys. Rev. B **73**, 104403 (2006).

[10] W. Xie, S. Populoh, K. Gałązka, X. Xiao, L. Sagarna, Y. Liu, M. Trottmann, J. He, and A. Weidenkaff, J. Appl. Phys. **115**, 103707 (2014).

[11] Z. Zheng, X. Su, R. Deng, C. Stoumpos, H. Xie, W. Liu, Y. Yan, S. Hao, C. Uher, C. Wolverton *et al.*, J. Am. Chem. Soc. **140**, 2673 (2018).

[12] S.-H. Wei and A. Zunger, Phys. Rev. B **35**, 2340 (1987).

[13] M. Krause and F. Bechstedt, J. Supercond. Nov. Magn. **26**, 1963 (2013).

[14] D. Kriegner, H. Reichlova, J. Grenzer, W. Schmidt, E. Ressouche, J. Godinho, T. Wagner, S. Y. Martin, A. B. Shick, V. V. Volobuev, G. Springholz, V. Holý, J. Wunderlich, T. Jungwirth, and K. Výborný, Phys. Rev. B **96**, 214418 (2017).

[15] S. Seki, T. Ideue, M. Kubota, Y. Kozuka, R. Takagi, M. Nakamura, Y. Kaneko, M. Kawasaki, and Y. Tokura, Phys. Rev. Lett. **115**, 266601 (2015).

[16] P. E. Blöchl, Phys. Rev. B **50**, 17953 (1994).

[17] G. Kresse and J. Furthmüller, Comput. Mater. Sci. **6**, 15 (1996).

[18] G. Kresse and J. Furthmüller, Phys. Rev. B **54**, 11169 (1996).

[19] C. Reig, V. Munoz, C. Gomez, C. Ferrer, and A. Segura, J. Cryst. Growth **223**, 349 (2001).

[20] M. E. Schlesinger, J. Phase Equilibria **19**, 591 (1998).

[21] J. P. Perdew, K. Burke, and M. Ernzerhof, Phys. Rev. Lett. **77**, 3865 (1996).

[22] H. J. Monkhorst and J. D. Pack, Phys. Rev. B **13**, 5188 (1976).

[23] S. L. Dudarev, G. A. Botton, S. Y. Savrasov, C. J. Humphreys, and A. P. Sutton, Phys. Rev. B **57**, 1505 (1998).

[24] M. Cococcioni and S. de Gironcoli, Phys. Rev. B **71**, 035105 (2005).

[25] R. S. Fishman, J. A. Fernandez-Baca, and T. Rõõm, *Spin-Wave Theory and Its Applications to Neutron Scattering and THz Spectroscopy* (Morgan & Claypool, San Raphael, CA, 2018).

[26] L. R. Walker and R. E. Walstedt, Phys. Rev. Lett. **38**, 514 (1977).

[27] J. M. Ziman, *Electrons and Phonons: The Theory of Transport Phenomena in Solids* (Oxford University Press, Oxford, UK, 2001).

[28] G. P. Srivastava, *The Physics of Phonons* (CRC, Boca Raton, FL, 1990).

[29] L. Lindsay, D. A. Broido, and T. L. Reinecke, Phys. Rev. B **87**, 165201 (2013).

[30] W. Li, J. Carrete, N. A. Katcho, and N. Mingo, Comput. Phys. Commun. **185**, 1747 (2014).

[31] R. Peierls, Ann. Phys. **396**, 121 (1930).

[32] D. A. Broido, M. Malorny, G. Birner, N. Mingo, and D. A. Stewart, Appl. Phys. Lett. **91**, 231922 (2007).

[33] L. Lindsay, Nanoscale Microscale Thermophys. Eng. **20**, 67 (2016).

[34] S.-i. Tamura, Phys. Rev. B **30**, 849 (1984).

[35] See Supplemental Material at http://link.aps.org/supplemental/10.1103/PhysRevMaterials.3.025403 for detailed computational exchange parameters, charge response, magnon dispersion and electronic band structure, and for experimental scattering functions and diffraction data.

[36] V. G. Kohn and A. I. Chumakov, Hyperfine Interact. **125**, 205 (2000); Ilya Sergueev (private communication).

[37] I. Sergueev, H.-C. Wille, R. P. Hermann, D. Bessas, Y. V. Shvyd'ko, M. Zajac, and R. Rüffer, J. Synchrotron Radiat. **18**, 802 (2011).

[38] S. J. Youn, B. I. Min, and A. J. Freeman, Phys. Status Solidi **241**, 1411 (2004).

[39] L. M. Sandratskii, R. F. Egorov, and A. A. Berdyshev, Phys. Status Solidi **104**, 103 (1981).

[40] R. M. Martin, *Electronic Structure: Basic Theory and Practical Methods* (Cambridge University Press, Cambridge, 2004).

[41] J. B. Goodenough, J. Phys. Chem. Solids **6**, 287 (1958).

[42] J. Kanamori, J. Phys. Chem. Solids **10**, 87 (1959).

[43] V. G. Vaks and N. E. Zein, J. Exp. Theor. Phys. **40**, 537 (1975).

[44] C. J. Fennie and K. M. Rabe, Phys. Rev. Lett. **96**, 205505 (2006).

[45] D. T. Morelli, V. Jovovic, and J. P. Heremans, Phys. Rev. Lett. **101**, 035901 (2008).

[46] K. Momma and F. Izumi, J. Appl. Crystallogr. **44**, 1272 (2011).

[47] Y. Ren, Q. Jiang, J. Yang, Y. Luo, D. Zhang, Y. Cheng, and Z. Zhou, J. Materiomics **2**, 172 (2016).